Feature-based characterization of motion-contaminated calcified plaques in cardiac multidetector CT

Martin King,[a] Maryellen L. Giger, Kenji Suzuki, and Xiaochuan Pan
Department of Radiology, Committee on Medical Physics, The University of Chicago, Chicago, Illinois 60637

In coronary calcium scoring, motion artifacts affecting calcified plaques are commonly characterized using descriptive terms, which incorporate an element of subjectivity in their interpretations. Quantitative indices may improve the objective characterization of these motion artifacts. In this paper, an automated method for generating 12 quantitative indices, i.e., features that characterize the motion artifacts affecting calcified plaques, is presented. This method consists of using the rapid phase-correlated region-of-interest (ROI) tracking algorithm for reconstructing ROI images of calcified plaques automatically from the projection data obtained during a cardiac scan, and applying methods for extracting features from these images. The 12 features include two dynamic, six morphological, and four intensity-based features. The two dynamic features are three-dimensional (3D) velocity and 3D acceleration. The six morphological features include edge-based volume, threshold-based volume, sphericity, irregularity, average margin gradient, and variance of margin gradient. The four intensity-based features are maximum intensity, mean intensity, minimum intensity, and standard deviation of intensity. The 12 features were extracted from 54 reconstructed sets of simulated four-dimensional images from the dynamic NCAT phantom involving six calcified plaques under nine heart rate/multi-sector gating combinations. In order to determine how well the 12 features correlated with a plaque motion index, which was derived from the trajectory of the plaque, partial correlation coefficients adjusted for heart rate, number of gated sectors, and mean feature values of the six plaques were calculated for all 12 features. Features exhibiting stronger correlations ($|r| \in [0.60, 1.00]$) with the motion index were 3D velocity, maximum intensity, and standard deviation of intensity. Features demonstrating stronger correlations ($|r| \in [0.60, 1.00]$) with other features mostly involved intensity-based features. Edge-based volume/irregularity and average margin gradient/variance of margin gradient were the only two feature pairs out of 12 with stronger correlations that did not involve intensity-based features. Automatically extracted features of the motion artifacts affecting calcified plaques in cardiac computed tomography images potentially can be used to develop models for predicting image assessability with respect to motion artifacts. © *2007 American Association of Physicists in Medicine.* [DOI: 10.1118/1.2794172]

Key words: cardiac CT, computed tomography, computer-aided diagnosis, feature extraction, image reconstruction, image analysis, assessability, calcium score

I. INTRODUCTION

Recent technological advances in cardiac multidetector computed tomography (CT) have revolutionized cardiac imaging. Faster gantry rotation times, increased numbers of detector rows, and reconstruction algorithms incorporating electrocardiogram (ECG)-correlated gating[1–5] have allowed for the generation of high quality images containing the entire three-dimensional (3D) volume of the heart from scan times lasting much less than the time of a single breath-hold. In many cases, the spatial and temporal resolutions of the reconstructed images are sufficient for the accurate delineation of coronary structures such as coronary artery segments and lesions such as noncalcified and calcified plaques. As a result, cardiac CT represents an emerging modality for applications such as coronary artery calcium (CAC) scoring and CT coronary angiography (CTA).[6,7]

However, even with these technological advances, image quality from cardiac CT often suffers from motion artifacts due to cardiac and respiratory movements. These motion artifacts appear because the projection data needed for reconstructing a cross-sectional image of the heart are not obtained within a small enough time window. In other words, temporal resolutions are not sufficient for "freezing" the motion of the heart, and the inconsistencies in the projection data may lead to streaks, blurs, positional changes, or general anatomical distortions in the reconstructed images.[8]

Motion artifacts are an important issue in cardiac CT because their presence may adversely affect the analysis of critical coronary structures. For example, for the case of CAC scoring, in which the amount of coronary calcium is quantified from noncontrast-enhanced CT images, motion artifacts can result in streaks, blurred lesion margins, doublings and discontinuities within calcified plaques. In CTA, the blurred margins, streaks, and discontinuities along the vessels from motion artifacts often make the task of detecting stenotic lesions difficult. Studies have shown that motion ar-

tifacts can increase the variability of coronary calcium scores[6,9–11] and reduce the diagnostic performance of CTA, even with recently introduced 64-slice CT scanners.[12–15]

Since motion artifacts can exhibit such a dramatic effect on image quality and overall diagnostic performance in cardiac CT, numerous schemes have been developed that associate types of motion artifacts to metrics representing the overall quality of the image. For example, in a study concerning the reproducibility of CAC scores, a five-point scale (1=no motion artifacts, 5=severe motion artifacts) was introduced in which calcified plaques with blurred lesion margins were assigned a score of 2, whereas plaques with tail-shaped and star-shaped artifacts were given respective scores of 3 and 4.[11]

Characterizing motion artifacts in terms of type and extent in a manner that fits within a designated scheme is not a straightforward task. For example, physicians may have different thresholds for deciding whether to designate a lesion margin as blurred. Furthermore, some physicians may be reluctant to characterize a calcified plaque exhibiting a small motion artifact as star-shaped (rating=4) when the extent of this artifact is much smaller than the large tail-shaped artifact (rating=3) in another image. Therefore, different physicians may arrive at different characterizations of the same motion artifacts affecting a given plaque. The main reasons for these difficulties are that these schemes use subjective descriptive terms to characterize motion artifacts, and physicians often have differing perceptions of how these descriptive terms relate with overall image quality. In addition, these characterizations are not easily quantifiable, such that the extent of a particular type of motion artifact commonly is not considered.

Quantitative indices have been developed and used for characterizing certain aspects of motion artifacts affecting coronary structures. In one study, the mean contrast of a calcified plaque was used for determining optimal phases for image interpretation.[16] In another study, the velocities of individual coronary landmarks specified by physicians were used for a similar purpose in CTA.[17] The indices used in these studies are useful, in that they represent quantitative metrics that provide objective characterizations of motion artifacts affecting a coronary structure. However, additional indices that can be used to quantify other aspects of the motion artifacts, such as morphological image distortions, need to be developed.

The purpose of this paper is to develop an automated method for obtaining a comprehensive list of indices, which will be referred to as *features*, that can be used to characterize the motion artifacts affecting a calcified plaque in noncontrast-enhanced cardiac CT images. The method includes both a rapid phase-correlated region-of-interest (RP-ROI) tracking algorithm for acquiring a four-dimensional (4D) set of ROI images centered on calcified plaques with minimal user interaction,[18] and mechanisms for segmenting and extracting features from these plaques.

The features included in this paper can be divided into the following three categories: dynamic features, morphological
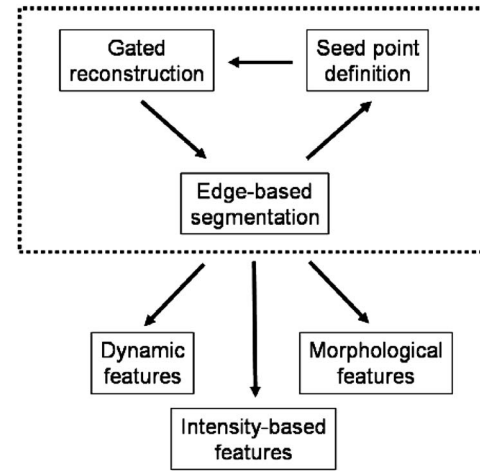

FIG. 1. Comprehensive scheme for obtaining phase-correlated features of calcified plaques. The dotted square encompasses portions of the scheme that are part of the rapid phase-correlated ROI (RP-ROI) tracking algorithm, which generates a 4D set of ROI images centered on calcified plaques.

features, and intensity-based features. These features will serve as computerized descriptors of a calcified plaque in a manner analogous to the features used for characterizing radiological lesions in computer-aided diagnosis applications.[19–21] Moreover, since these features can be extracted from images of plaques at different cardiac phases, they will be *temporally phase-correlated* features. The application of these features in a computerized scheme for evaluating the quality of calcified plaques in cardiac CT images with respect to motion artifacts is discussed elsewhere.[22]

This paper is organized as follows. In Sec. II, the materials and methods are provided. Results are presented in Sec. III, and a discussion of these results is included in Sec. IV.

II. MATERIALS AND METHODS

In this section, the NURBS-based cardiac-torso (NCAT) phantom[16,23–25] used in the simulation studies is first discussed. The RP-ROI tracking algorithm for generating a 4D set of ROI images centered on the calcified plaques and an edge-based method for segmenting calcified plaques in these images are then presented. Methods for extracting the 12 features characterizing calcified plaques are described. Finally, techniques for evaluating these features are discussed. A simple flow chart of these steps is shown in Fig. 1.

II.A. Materials
II.A.1. NCAT phantom

The digital NCAT phantom was used to produce a temporal series of 3D attenuation maps of the thorax at 32 cardiac phases evenly spaced throughout the cardiac cycle.[23–25] No respiratory motion was present, and contrast agent was not included in the cardiac chambers or coronary vasculature. A voxel size of 0.6 mm, which falls within the range of spatial resolutions for cardiac CT scanners, was used for all maps.
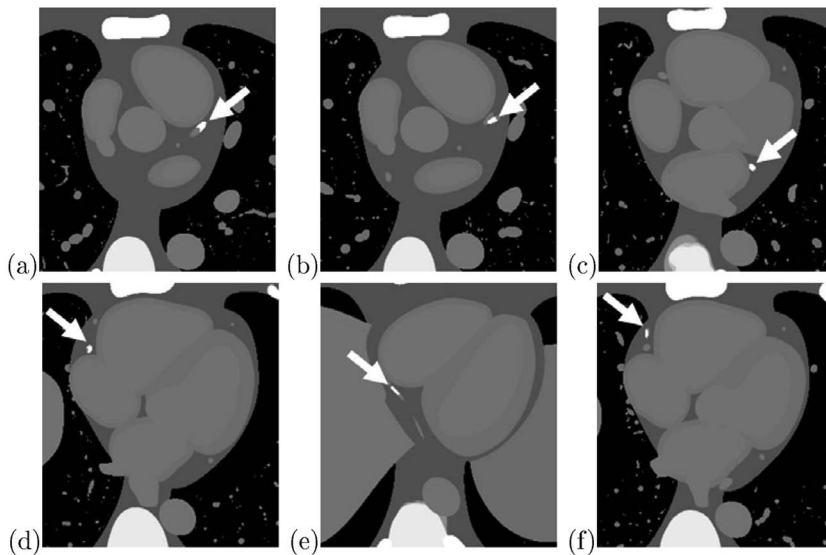
FIG. 2. Transverse slices of the NCAT phantom through the following calcified plaques: (a) LAD1, (b) LAD2, (c) LCX, (d) RCA1, (e) RCA2, and (f) RCA3. In each image, a solid white arrow points to the calcified plaque. L: 50 HU/W: 400 HU.

Generating 3D attenuation maps of the thorax at this voxel size was extremely computationally demanding, and so the voxel size was not decreased any further.

Separate attenuation maps were also generated for six calcified coronary plaques. Two were located in the left anterior descending (LAD) artery; one was located in the left circumflex (LCX) artery; and three were present in the right coronary artery (RCA). These maps were constructed at the same cardiac phases as those used above for the thorax, but with a voxel size of 0.2 mm. Since this study was concerned with characterizing calcified plaques, this higher spatial resolution was used to decrease the likelihood that discretization errors from "voxelizing" the plaque prior to projection data acquisition would affect the extracted features. Examples of transverse slices of the NCAT phantom with the calcified plaques labeled LAD1, LAD2, LCX, RCA1, RCA2, and RCA3 are shown in Fig. 2.

II.A.2. Projection data acquisition

Projection datasets of the NCAT phantom were acquired using a circular cone-beam scanning geometry defined by a focal length of 57 cm, a source-to-detector distance of 104 cm, and a 50 cm reconstruction field of view (FOV). The flat panel detector consisted of a 1024 by 84 array with an isotropic square bin size of 0.54 mm when scaled to isocenter. The gantry rotation time (RT) was set to 0.4 s.

Projection datasets were acquired at heart rates of 50, 66, 80, and 90 bpm over multiple cardiac cycles. A cardiac phase delay algorithm[17] was incorporated in order to take into account the effects of different heart rates on the lengths of phases within the cardiac cycle. Since the attenuation maps for the thorax and calcified plaque components of the NCAT phantom were generated at different spatial resolutions, projection datasets of the thorax and calcified plaques were acquired independently and then summed together. Poisson noise based on an initial intensity of 1.0×10^6 photons/

detector element was added to the summed projection datasets. Photon intensities of similar orders have been used in other CT simulation studies.[26,27]

II.B. Rapid phase-correlated ROI (RP-ROI) tracking algorithm

In this section, an automated method for rapidly acquiring a temporal series of phase-correlated ROI images centered on a moving calcified plaque is presented. This method, which we refer to as the rapid phase-correlated ROI tracking algorithm, requires two inputs for obtaining a time-resolved 4D set of ROI images. First, the projection dataset is acquired with the calcified plaque remaining in the reconstructable FOV over all cardiac phases of interest. Second, the user specifies the location (seed point) of the plaque at an initial phase. The rest of the method for generating the 4D set of plaque images is automated.[18]

The RP-ROI algorithm is based on the reconstruction, segmentation, and seed point definition framework included in Fig. 1. In short, an initial image of the entire phantom is reconstructed from the projection dataset at an initial phase. A seed point is placed by the user on the calcified coronary plaque. A cubic ROI image centered on the seed point at an advanced cardiac phase is then obtained by using a reconstruction algorithm incorporating either single-sector or multi-sector gating. The calcified plaque is segmented within this ROI image using edge-based methods. Finally, the center of mass (geometric center or centroid) of the calcified plaque is calculated from the segmentation results and defined as the seed point. The reconstruction, segmentation, and seed point definition processes are then repeated over advancing cardiac phases until a 4D dataset of phase-correlated ROI images is obtained over all phases of interest. The three components included in the framework are described in more detail below.
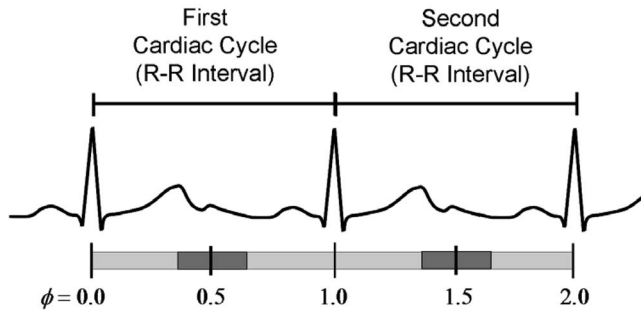
FIG. 3. Schematic depicting how cardiac phase ϕ is defined with respect to the %R-R interval over two cardiac cycles. Phases ϕ of 0.5 and 1.5 both correspond to the same %R-R interval of 50%. The shaded boxes centered on both of these phases depict the short-scan phase interval $[\phi_{\min}, \phi_{\max}]$ needed for reconstructing images at average phases $\bar{\phi} = (\phi_{\min} + \phi_{\max})/2$ of 0.5 and 1.5. In two-sector reconstruction, data from both shaded areas are used for reconstructing images corresponding to an average phase $\bar{\phi}$ of 0.5.

II.B.1. Phase-correlated image reconstruction

Phase-correlated (gated) reconstruction refers to the acquisition of images corresponding to specific phases within the cardiac cycle. For the RP-ROI algorithm, images are reconstructed with a weighted filtered backprojection algorithm.[28,29] This algorithm is used instead of the conventional Feldkamp, Davis, and Kress algorithm[30,31] because the weighting function, which takes into account the redundancy of the projection data in the plane of the circular source trajectory, is applied after the filtration step. Therefore, the projection data obtained at a scanning angle need to be filtered only once, even though the filtered data can be used to reconstruct multiple images over a range of cardiac phases. As is commonly done in cardiac imaging, a weighting function, which requires data spanning a short-scan angular range $\Delta\lambda = \pi + $ fan angle, is used.

The percent R-R interval (%R-R interval) is commonly used for designating phases within a given cardiac cycle, which spans one heartbeat and covers phases of cardiac contraction (systole) and expansion (diastole). However, in order to designate phases across multiple cardiac cycles, our study uses the symbol ϕ, which is related to the %R-R interval by the expression %R-R $= \phi \mod 1$. Thus, cardiac phases with equivalent %R-R intervals but from different cardiac cycles, such as phases of $\phi = 0.5$ and $\phi = 1.5$, can be differentiated from one another (see Fig. 3).

Since each image is reconstructed from a projection data sector covering a short-scan angular range, each reconstructed image also corresponds to a short-scan phase interval $[\phi_{\min}, \phi_{\max}]$, which is centered on the average cardiac phase $\bar{\phi} = (\phi_{\min} + \phi_{\max})/2$. The average cardiac phase $\bar{\phi}$ of a reconstructed image is referred to as phase for brevity in the discussions that follow. The range spanned by the phase interval $\Delta\phi = \phi_{\max} - \phi_{\min}$ corresponds to the time window for single-sector reconstruction $t_r = RT \times \Delta\lambda/2\pi$.

Multi-sector reconstruction is a method commonly used for improving the temporal resolution and suppressing motion artifacts for patients with stable heart rates.[2–4] This method consists of using phase-correlated data sectors from two or more cardiac cycles for reconstructing a single image, as shown in Fig. 3. The gated data sectors have overlapping %R-R intervals, such that the range of the cardiac phase interval $\Delta\phi$ is decreased. For this algorithm, multi-sector reconstruction is performed in a manner similar to that described in Ref. 32.

II.B.2. Edge-based segmentation

In our previous study, the RP-ROI algorithm utilized a threshold-based segmentation algorithm for defining seed points corresponding to the locations of calcified plaques.[18] This segmentation method involved thresholding the plaque at 130 HU. Although this method was reliable for larger plaques undergoing lower levels of motion, it often failed to define accurate seed points for smaller plaques undergoing higher levels of motion, such as those located in the right coronary arteries. As a result, the RP-ROI tracking algorithm often failed to retain the plaque within the reconstructed ROI throughout the cardiac phases of interest.

In this study, an edge-based segmentation method is incorporated into the RP-ROI algorithm. This method is used not only for defining more accurate seed points for plaques undergoing a high degree of motion, but also is capable of better capturing the motion artifacts affecting calcified plaques in general. As a result, the features used to characterize motion artifacts affecting calcified plaques are extracted directly from the segmentation results.

The segmentation method is illustrated in Fig. 4, and is discussed as follows. First, voxels corresponding to known extraneous structures with attenuation values above 130 HU, such as the sternum, are removed from the reconstructed image. Then, transverse slices of the reconstructed volumetric image are passed through two edge-based filters. The first is a Laplacian filter, which is applied in order to extract prominent edges within each entire slice. A constant parameter I_{Lap} is used to threshold the Laplacian filtered image in order to create a binary mask. Since this type of edge-based filter is extremely sensitive to image noise, the original image is smoothed before being processed by the Laplacian filter. Smoothing is performed with a 3×3 pixel boxcar filter.

The second edge-based filter is a Sobel filter, which is used to extract a region covering an area somewhat larger than the plaque and its associated motion artifacts. A constant parameter I_{Sob} is also used in order to create a binary mask for the Sobel filtered image. The following three steps are then taken to process the resulting Sobel filtered image. First, regions of the Sobel binary mask are identified through connected-component labeling based on 26-point connectivity. Regions corresponding to prominent edges between the heart and lung are eliminated based on the criteria that these regions have mean intensities below 0 HU. Second, a contingency check is performed to ensure that a minimum of number of voxels N_{Sob} are included in the Sobel binary mask. If the number of voxels is less than N_{Sob}, histogram analysis is performed to select the N_{Sob} voxels with the greatest values from the Sobel filtered image. These voxels are
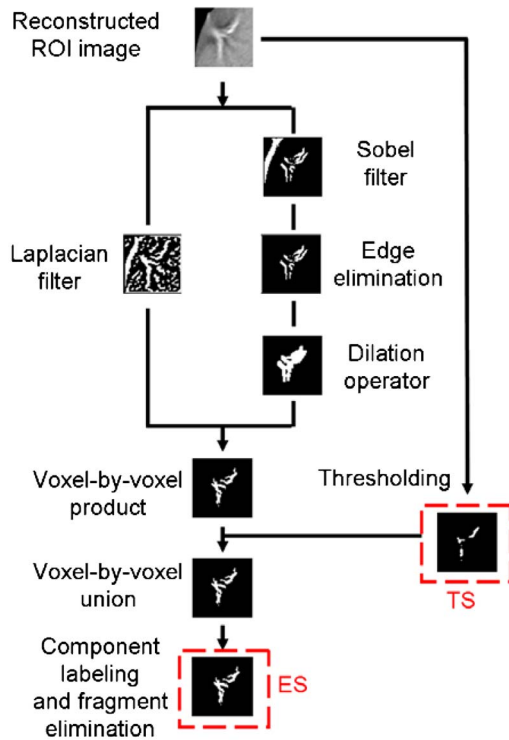
FIG. 4. Flow chart for the edge-based segmentation method described in Sec. II B 2. TS and ES stand for threshold-based (130 HU) and edge-based segmentation results, which are enclosed by the dashed squares. Edge elimination refers to the removal of prominent edges between the heart and lung. Fragment elimination refers to the removal of volumetric fragments with mean intensities, numbers of voxels, and center of mass distances less than their defined cutoffs. Notice how the motion artifacts are better captured in ES than in TS.

TABLE I. Nine heart rate/multi-sector gating combinations used for reconstructing images of the calcified plaques using the RP-ROI algorithm.

Label	HR/Multi-Sector Gating Combination
H50/G1	Heart rate 50 bpm/Single-sector gating
H66/G1	Heart rate 66 bpm/Single-sector gating
H66/G2	Heart rate 66 pbm/Two-sector gating
H80/G1	Heart rate 80 bpm/Single-sector gating
H80/G2	Heart rate 80 bpm/Two-sector gating
H80/G3	Heart rate 80 bpm/Three-sector gating
H90/G1	Heart rate 90 bpm/Single-sector gating
H90/G2	Heart rate 90 pbm/Two-sector gating
H90/G3	Heart rate 90 bpm/Three-sector gating

included in the Sobel binary mask. Third, since the binary mask of the Sobel-filtered image often contains holes within the central region of the plaque, a dilation operator with a cross-shaped structuring element is used to expand this binary mask. The deletion of regions in the Sobel binary mask corresponding to prominent edges between the heart and lung is necessary prior to performing this dilation step. Otherwise, for cases in which the plaque is very close to the edge of the heart, the dilation step would cause these two regions to merge and subsequently become deleted. Further details of the segmentation methods discussed above can be found in image processing textbooks.[33,34]

The binary mask from the Laplacian filter and the dilated binary mask from the Sobel filter are then multiplied (voxel-by-voxel product) together in order to obtain a third binary mask of the calcified plaque. In order to ensure that no portions of a calcified plaque with attenuation values greater than 130 HU are missed, a voxel-by-voxel union is performed between this third binary mask and a fourth mask obtained by thresholding the reconstructed slice at 130 HU with the known extraneous structures such as the sternum removed.

Connected-component labeling based on 26-point connectivity is then applied across all slices of the edge-based segmentation result in order to identify distinctly separated

volumetric fragments. Fragments with mean intensities, voxel numbers, and center of mass distances from the seed point, which are less than mean intensity $\bar{I}_c$, voxel number $N_{edge,c}$ and center of mass distance $DIST_c$ cutoff values, are removed in order to obtain the final segmentation result. Fragments with these properties are often extracted from edges that are not part of calcified plaques or their associated motion artifacts, and removing these fragments reduces the amount of clutter in the final segmentation result.

The edge-based segmentation methodology described above requires six empirically determined parameters to be specified. Two parameters are the I_{Lap} and I_{Sob} threshold values used for obtaining the binary masks from the Laplacian filtered and Sobel filtered images, respectively. The third is the minimum number of voxels included in the Sobel segmentation result prior to dilation, N_{Sob}. The final three are the mean intensity $\bar{I}_c$, voxel number $N_{edge,c}$, and distance $DIST_c$ cutoffs used for eliminating volumetric fragments before obtaining the final segmentation result.

II.B.3. Seed point definition

The seed point of the plaque at the next cardiac phase is defined by calculating the center of mass of the image region corresponding to the edge-based segmentation result. If no fragments are present in the edge-based segmentation result, the seed point is left unchanged. If the plaque no longer remains within the reconstructed ROI after a certain phase due to inaccurate seed points, the RP-ROI algorithm is said to have failed. In this case, a new seed point is defined at the first cardiac phase in which the computer's segmentation algorithm is capable of clearly identifying the plaque.

II.B.4. Implementation of the RP-ROI algorithm

In this study, the RP-ROI algorithm was applied to the six calcified plaques using the nine heart rate/multi-sector gating combinations shown in Table I. These nine combinations spanned four heart rates of 50, 66, 80, and 90 bpm. Single-sector (G1) gating was used for all heart rates, and two-sector (G2) and three-sector (G3) gating were implemented at and above heart rates of 66 and 80 bpm, respectively. In total, 54 4D image sets were acquired. Images were reconstructed at advancing cardiac phase intervals $\Delta\bar{\phi} \approx 0.01$ over

TABLE II. Twelve features characterizing the motion-contaminated calcified plaques.

Feature	Feature type	Feature description
VEL	Dynamic	3D velocity
ACC	Dynamic	3D acceleration
VOL-E	Morphological	Edge-based volume
VOL-T	Morphological	Threshold-based volume
SPHER	Morphological	Sphericity
IRREG	Morphological	Irregularity
MG	Morphological	Margin gradient
VMG	Morphological	Variance of margin gradient
MAX INT	Intensity-based	Maximum intensity
MEAN INT	Intensity-based	Mean intensity
MIN INT	Intensity-based	Minimum intensity
STD INT	Intensity-based	Standard deviation of intensity

250 phases on 24.22 mm cubic ROIs with voxel sizes of 0.39 mm. This voxel size was chosen based on the reconstruction of 512×512 cardiac CT slices covering a 200 mm FOV. Note that this voxel size was almost twice as large as the original voxel size of 0.2 mm used for generating the calcified plaques.

The following parameters were used for all edge-based segmentations in the RP-ROI algorithm: $I_{Lap}=-10$ HU; $I_{Sob}=-708$ HU; $N_{Sob}=50$ voxels; $\bar{I}_c=50$ HU; $N_{edge,c}=50$ voxels; and $DIST_c=15$ mm. The RCA1 plaque moving at 90 bpm underwent a substantial amount of motion throughout the cardiac cycle and was used for tuning these parameters. Although the RCA3 plaque was successfully tracked using the above parameters, visual assessments showed that these edge-based segmentations often failed to capture the morphologies of the motion artifacts affecting this plaque, especially at higher heart rates. As a result, the RCA3 plaques were re-segmented with I_{Lap} and I_{Sob} threshold values of -5 HU and -776 HU. Note that segmentation results were not compared to radiologists' outlines due to the potential for large inter-observer variability in the outlining of these motion artifacts.

II.C. Feature extraction

In this section, the extraction of phase-correlated features from each of the 4D image sets is described. As shown in Fig. 1, extracted features are categorized into dynamic features, morphological features, and intensity-based features. These features are listed in Table II.

II.C.1. Dynamic features

The two dynamic features are 3D velocity (VEL) and 3D acceleration (ACC). The seed points obtained from the RP-ROI tracking algorithm are used as phase-correlated positional vectors for the plaque. From these positional vectors, the 3D displacement of the plaque from a central point, as well as the 3D velocity and 3D acceleration features are calculated. The 3D velocity is obtained by smoothing each Car-

tesian component of the positional vectors using a box-car filter over cardiac phase $\bar{\phi}$, calculating the instantaneous velocity vectors by taking the first derivative of each Cartesian component, and then obtaining the norm of these instantaneous velocity vectors. The feature 3D acceleration is obtained from the velocity vectors in an analogous manner. For this study, a boxcar filter width of 10 is used in all calculations.

II.C.2. Morphological features

Two of the morphological features are volume descriptors. The first descriptor of edge-based volume (VOL-E) is simply the volume of the edge-based segmentation result. This feature is calculated by summing the number of voxels included in the edge-based segmentation result, and multiplying this number by the voxel volume. The second descriptor of threshold-based volume (VOL-T) is the volume of a segmentation result obtained by counting the number of voxels included in the edge-based segmentation result with intensity values above or equal to 130 HU. This descriptor is closely related to volume-based methods for quantifying coronary calcium.[35]

Shape-based features of sphericity (SPHER) and irregularity (IRREG) are included in the set of morphological features. Sphericity is defined as the ratio of the lesion volume within a sphere of effective diameter d_{eff} to the entire lesion volume. The center of mass of the edge-based segmentation result is used as the central point for the sphere. The effective diameter d_{eff} is defined as

$$d_{eff} = 2\sqrt[3]{\frac{3 \cdot \text{Lesion volume}}{4\pi}}. \tag{1}$$

The sphericity feature ranges from zero to one, in which a value of one indicates that the plaque is a perfect sphere. The irregularity feature is given by $1 - \pi d_{eff}^2/$ surface area, where the surface area is defined as the number of voxels included in the segmentation result that have at least one adjacent voxel not included in the segmentation result. Adjacent voxels are determined based on 26-point connectivity. The irregularity feature also ranges from zero to one, in which a value of zero indicates a perfect sphere.

Two features are related to margin sharpness.[19] The average margin gradient (MG) of the plaque is defined as the mean of the plaque margins normalized by the mean intensities along the margins. The variance of margin gradient (VMG) is the variance of the plaque margins normalized by the square of the mean intensities along the margins. Plaque margins are voxels that belong to the surfaces of the edge-based segmentation results and contribute to plaque surface areas in the irregularity calculation discussed above.

II.C.3. Intensity-based features

Four intensity-based features based on the maximum intensity (MAX INT), mean intensity (MEAN INT), minimum intensity (MIN INT), and standard deviation of intensity (STD INT) of voxels present within the edge-based segmentation result are defined.
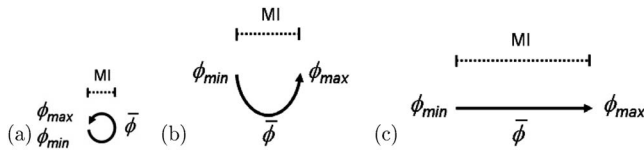
FIG. 5. Plaque motion index MI under three possible plaque trajectories (solid arrow) during the phase interval $[\phi_{min}, \phi_{max}]$. Note that images are indexed by the average cardiac phase $\bar{\phi} = (\phi_{min} + \phi_{max})/2$. The motion index is defined as the maximum distance between any two points for a given plaque trajectory mapped out over this phase interval.

II.D. Evaluation methods

The dynamic, morphological, and intensity-based features were extracted from the 4D image sets obtained through the RP-ROI algorithm and evaluated in the following manner. Dynamic features were evaluated by comparing how well these features matched with their actual values, as determined from the NCAT phantom. In addition, root mean square (rms) errors were used to quantitatively determine the accuracies of the phase-correlated positional vectors, which were used to calculate the 3D velocity and 3D acceleration features. The rms errors for a given 4D image set were calculated for each of the three Cartesian components of the positional vectors. The norm of these three errors was then reported as the rms error for a given plaque and heart rate/gating combination.

Morphological and intensity-based features were evaluated by comparing these feature values to reconstructed images of the six plaques. The relationships between these features and cardiac phase were also examined for different plaques, heart rates, and gating combinations. Strengths of associations between these features and the plaque motion index discussed below were assessed as well.

II.D.1. Plaque motion index

The plaque motion index, which served as a truth for evaluating individual features, is a metric that quantifies the amount of plaque motion pertaining to an image at a cardiac phase $\bar{\phi} = (\phi_{min} + \phi_{max})/2$. This motion index (MI) is defined as the maximum distance between any two points of the actual plaque trajectory mapped out over the phase interval $[\phi_{min}, \phi_{max}]$ used for reconstruction divided by the time window required for single-sector reconstruction t_r. Figure 5 shows examples of this motion index for three plaque trajectories.
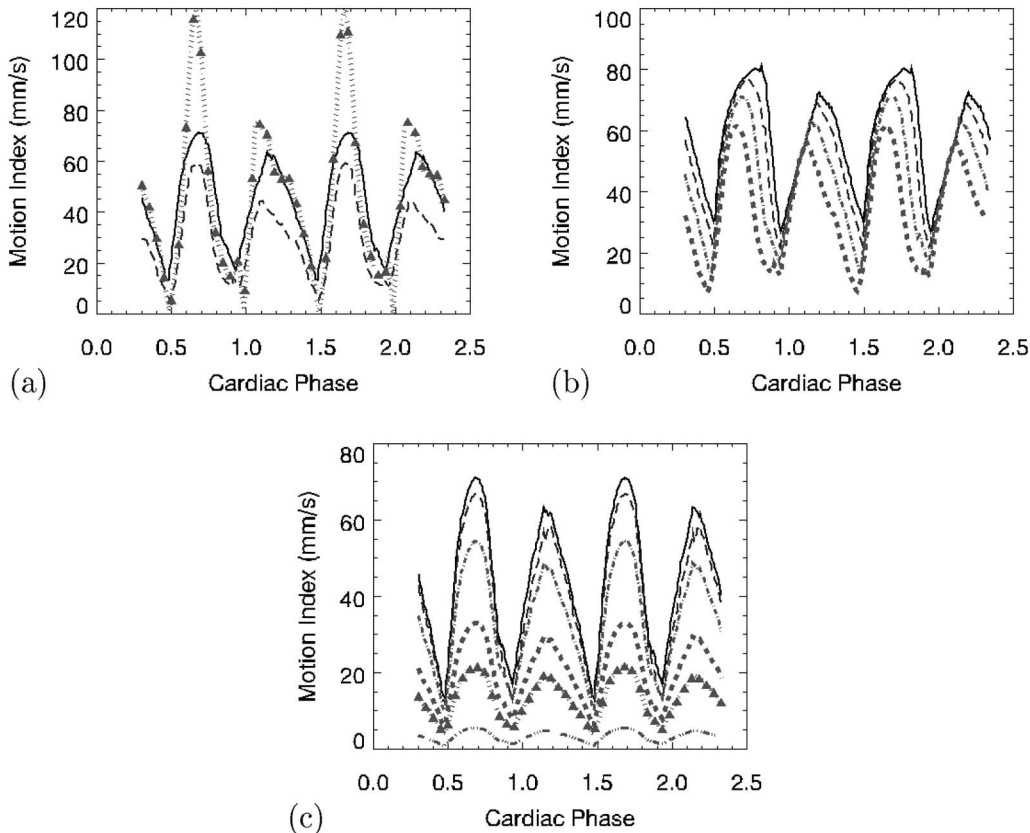
FIG. 6. Plaque motion indices of selected 4D image sets. In (a), motion indices are obtained from images of the RCA1 plaque with H66/G1 (solid line) and H66/G2 (dashed line) combinations, respectively. The hashed line with triangles represents the plaque's true instantaneous velocity. In (b), motion indices corresponding to the RCA1 plaque with G1 reconstructions are plotted for heart rates of 90 bpm (solid line), 80 bpm (thin dashed line), 66 bpm (dash-dot-dashed line), and 50 bpm (thick dashed line). In (c), motion indices are plotted for the following plaques under the H66/G1 combination: RCA1 (solid line), RCA3 (thin dashed line), RCA2 (dash-dot-dashed line), LAD2 (thick dashed line), LCX (hashed line with triangles), and LAD1 plaques (dash-dot-dot-dot-dashed line).

FIG. 7. Phase-correlated ROI reconstructions of the (a) LAD2 and (b) RCA1 plaques (H66/G1) at advancing cardiac phase intervals $\Delta\bar{\phi}\approx 0.01$. The phase for a given image is obtained by adding the numbers next to the rows and columns corresponding to the image. L: 50 HU/W: 400 HU.
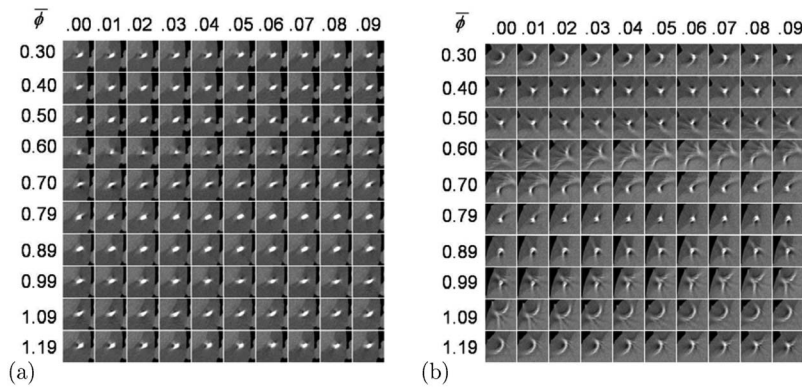
The reason that the motion index is used instead of instantaneous plaque velocity is that the motion index incorporates information from the entire plaque trajectory corresponding to the phase interval $[\phi_{min}, \phi_{max}]$. For example, if the plaque undergoes an abrupt change in direction, the motion index does not approach zero as it would if instantaneous velocity were used. Furthermore, instantaneous velocity would provide nearly equivalent values for images of the same plaque reconstructed with single-sector and two-sector gating. The plaque motion index, on the other hand, would always provide lower motion indices for images obtained with two-sector gating, because the range of the phase interval $\Delta\phi = \phi_{max} - \phi_{min}$ is shorter for two-sector gating than it is for single-sector gating. As a result, the plaque motion index would be a better indicator of image quality with respect to motion artifacts.

Graphs between plaque motion indices and cardiac phase are included in Fig. 6. As seen in the first graph, which shows motion indices for the RCA1 plaque at 66 bpm, plaque motion indices for the G2 reconstructions were lower than those for the G1 reconstructions. This phenomenon was expected due to the smaller phase intervals $\Delta\phi$ covered by the G2 reconstructions. In addition, the peaks and valleys for both G1 and G2 curves tended to correlate well with those found in the instantaneous velocity curve. The graph shown in Fig. 6(b) compares motion indices for different heart rates corresponding to the G1 reconstructions of the RCA1 plaque. As expected, motion indices were greater for higher heart rates. The plot in Fig. 6(c) illustrates how the plaque motion indices varied between each of the six calcified plaques with

the same H66/G1 combination. As seen in this figure, motion indices for the plaques in the right coronary arteries were much greater than those in the left coronary arteries.

II.D.2. Correlations of features to plaque motion

In order to identify features that demonstrated noticeable nonlinear relationships with the plaque motion index, scatter plots, residual scatter plots, and histograms were created for features corresponding to individual plaques. For features exhibiting strong nonlinear relationships for multiple plaques, log, square root, and power transformations were visually examined to determine if these transformations improved linearity. Transformations involving the square roots of 3D velocity and 3D acceleration, and the square of sphericity, managed to improve linearity for many plaques and were used in all subsequent calculations.

Partial correlation coefficients[36] were used to analyze strengths of associations between the 12 features and the plaque motion index. The partial correlation coefficients were calculated for each of the plaques individually and across all six plaques. By using partial correlation coefficients, correlations between features and motion indices were adjusted for differences in heart rate, number of gated sectors, and mean values of features between different calcified plaques. Adjusting for these three factors was important, since they served as covariates that could confound the relationship between a given feature and the motion index. In order to adjust for differences in mean values of features
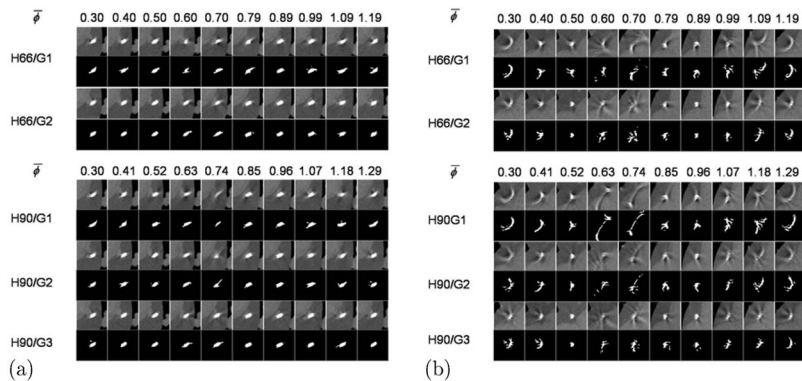

FIG. 8. Sample reconstructions and segmentations for the (a) LAD2 and (b) RCA1 plaques for different heart rate/gating (H/G) combinations, as specified in Table I.
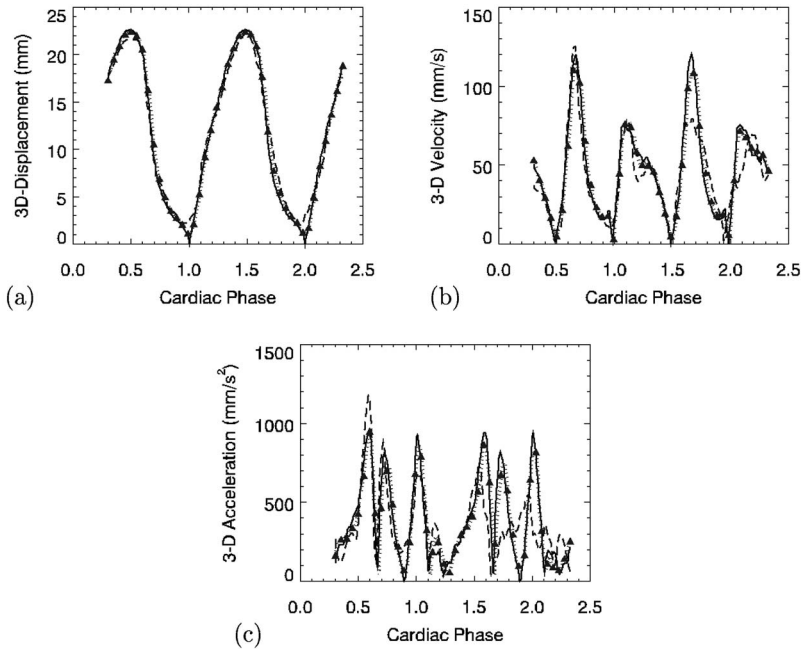
FIG. 9. Dynamic measurements of (a) 3D displacement, (b) 3D velocity (VEL), and (c) 3D acceleration (ACC) vs cardiac phase for the RCA1 plaque moving at 66 bpm. In each plot, the solid line represents actual values; the dashed line represents results obtained with single-sector gating (G1); and the hashed line with triangles represents results obtained with two-sector gating (G2).

between the different plaques, five binary-valued dummy variables were included in the calculations of the partial correlation coefficients across all six plaques.[37]

Relationships between pairs of individual features were also evaluated by calculating pairwise partial correlation coefficients for the 12 features across all six plaques. Pairs of features exhibiting stronger correlations ($|r| \in [0.60, 1.00]$) were noted. For the calculation of all partial correlation coefficients, the number of samples per plaque was 1854 (nine HR/gating combinations * 206 phases).

III. RESULTS

The RP-ROI algorithm successfully retained the plaque within the reconstructed ROI over all cardiac phases of interest for the six calcified plaques obtained with the nine heart rate/gating combinations. However, for the RCA3 plaque with the H80/G3 combination, the RP-ROI algorithm was unable to detect the plaque for seven consecutive reconstructions due to the faintness of this plaque during phases of high cardiac motion. As a result, no new seed points were defined for these reconstructions. Fortunately, the segmentation algorithm was capable of finding the plaque on the eighth reconstruction without user intervention. Examples of phase-correlated reconstructions of the LAD2 and RCA1 plaques moving at 66 bpm with single-sector gating are shown in Fig. 7. As seen in this figure, the morphologies of motion artifacts for a given plaque gradually transformed over advancing cardiac phases.

Figure 8 shows reconstructions and segmentations of the LAD2 and RCA1 plaques at all multi-sector gating combinations involving heart rates of 66 and 90 bpm. As expected, motion artifacts became more pronounced at higher heart rates. Also, increasing the number of sectors for gating managed to suppress motion artifacts over many cardiac phases.

Instead of the usual streaks and blurs, motion artifacts became more contained when multi-sector gating was implemented. However, for phases of high cardiac motion, the motion artifacts were still noticeable and exhibited a smudge-like appearance.

III.A. Dynamic features

Graphs showing the relationships of measured and actual 3D displacement, 3D velocity, and 3D acceleration values to cardiac phase for the RCA1 plaque moving at 66 bpm are shown in Fig. 9. In general, measurements obtained from the two-sector (G2) reconstructions were more accurate than those from the single-sector (G1) reconstructions. In addition, the 3D displacement plots seemed to be the most accurate, whereas the 3D acceleration plots seemed to be the least accurate. These results were expected, as small deviations in measured positions became amplified in the derivative operations used to obtain the 3D velocity and 3D acceleration values.

Figure 10 shows the relationships of rms errors of position for the plaques under different heart rate/gating combinations. The rms errors for the three plaques in the right coronary arteries were much greater in general than those in the left coronary arteries. Also, rms errors tended to become smaller as heart rates decreased and the numbers of sectors used for reconstruction increased. However, in certain cases, rms errors for the H90/G2 and H90/G3 reconstructions were lower than those for the H80/G2 and H80/G3 reconstructions, respectively. A likely explanation is that the temporal resolutions for the G2 and G3 reconstructions at 90 bpm were better than the corresponding temporal resolutions at 80 bpm due to greater desynchronization of the 0.4 s gantry rotation time and the heart rate at 90 bpm.[4] The rms error of the H80/G3 combination for the RCA3 plaque was substantially higher than the rms error for the H80/G2 combination
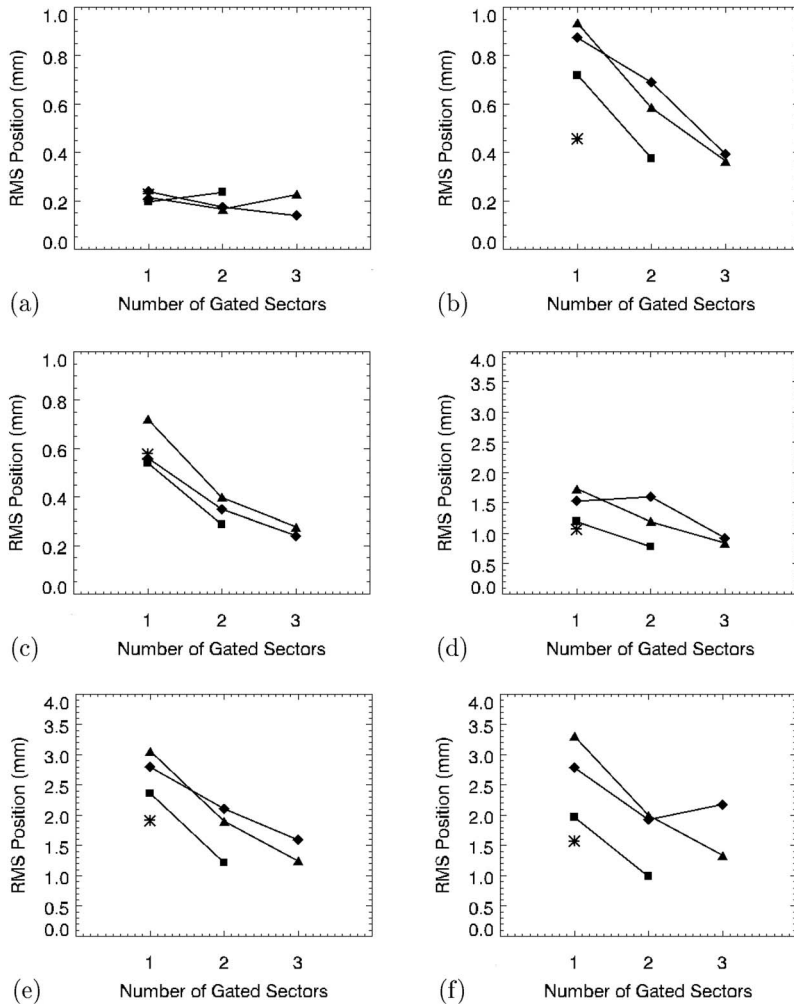
FIG. 10. Root-mean-square (rms) error plots of plaque position vs the number of gated sectors for the (a) LAD1, (b) LAD2, (c) LCX, (d) RCA1, (e) RCA2, and (f) RCA3 plaques at heart rates of 50 (asterisk), 66 (square), 80 (diamond), and 90 (triangle) bpm. Note the differing scales for rms error between plots in (a)–(c) and (d)–(f).

since, as discussed earlier, the RP-ROI algorithm failed to detect the plaque over seven consecutive phases and the seed points were left unchanged during these phases.

III.B. Morphological and intensity-based features

In Figs. 11 and 12, reconstructions and segmentations of the six calcified plaques with the 66 bpm/single-sector gating combination along with corresponding values of selected features are shown for specified phases over two cardiac cycles. These figures are included in order to illustrate how values for the selected features were associated with the different types of motion artifacts affecting each of the calcified plaques. For a given plaque, values for a specific feature varied over a wide range depending on the extents to which motion artifacts affected the plaque. In addition, plaques with lower motion indices tended to exhibit lower levels of motion artifacts than plaques with higher motion indices.

Figure 13 shows graphs of the following morphological and intensity-based features obtained from G1 and G2 reconstructions of the RCA1 plaque at 66 bpm: edge-based volume, threshold-based volume, sphericity, irregularity, mean intensity, and average margin gradient. Note that all of these features exhibited a semiperiodic nature over the two cardiac

cycles shown. The periodicity of the features tended to correlate with the systolic and diastolic phases of the heart, and many of the features obtained from the G2 reconstructions seemed to exhibit a more periodic nature than those from the G1 reconstructions. In addition, feature values at equivalent %R-R intervals often differed between the two cycles. Motion artifacts of corresponding plaques also appeared quite differently, as shown in Figs. 11 and 12. These results demonstrate that even though the plaque underwent the exact same trajectory between the two periods, the differing orientations of the rotating gantry with respect to the moving plaque between the two cardiac cycles were sufficient for generating noticeably different motion artifacts.

The values for features between different plaques also varied considerably. Table III shows means and standard deviations of the 12 features using values from all heart rate/gating combinations for each of the six calcified plaques. The data in this table show that different plaques had different properties in terms of dynamics, size, shape, intensity, and margin sharpness. The RCA2 plaque, for example, covered a much smaller volume on average than the other five plaques. The standard deviations of individual features also differed between plaques.

$\bar{\phi}$	0.30	0.50	0.70	0.89	1.09	1.29	1.49	1.68	1.88	2.08
Rec										
Seg										
VEL	3.4	0.6	4.3	1.6	3.8	5.5	0.6	8.6	2.2	4.4
VOL-E	49.4	45.1	49.4	42.2	47.4	47.0	44.6	58.0	43.7	49.7
SPHER	0.63	0.63	0.63	0.65	0.63	0.64	0.62	0.62	0.66	0.63
MEAN INT	234	235	220	235	222	225	245	194	227	226
MG	3.69	3.76	3.77	3.80	3.93	3.86	3.79	3.49	3.95	3.61
MI	3.5	1.6	5.5	1.7	4.2	3.7	1.4	5.5	1.9	4.0

(a)

$\bar{\phi}$	0.30	0.50	0.70	0.89	1.09	1.29	1.49	1.68	1.88	2.08
Rec										
Seg										
VEL	17.4	1.6	22.6	6.2	18.6	29.9	1.6	56.6	14.2	27.5
VOL-E	45.3	32.8	53.8	36.5	53.8	49.4	32.5	69.4	36.5	63.1
SPHER	0.47	0.59	0.44	0.61	0.47	0.48	0.60	0.40	0.61	0.44
MEAN INT	181	216	154	213	170	168	221	137	212	156
MG	3.44	3.94	3.20	3.63	3.25	3.32	4.07	2.88	3.68	2.87
MI	21.2	9.9	32.9	10.3	25.0	22.0	8.4	33.0	11.3	24.2

(b)

$\bar{\phi}$	0.30	0.50	0.70	0.89	1.09	1.29	1.49	1.68	1.88	2.08
Rec										
Seg										
VEL	17.5	7.4	30.2	4.5	13.3	13.3	2.6	22.0	8.5	16.2
VOL-E	62.9	38.9	82.4	37.3	57.3	46.6	40.0	76.5	39.9	68.2
SPHER	0.57	0.60	0.52	0.59	0.56	0.59	0.60	0.56	0.62	0.56
MEAN INT	174	233	149	230	172	197	234	153	224	166
MG	3.06	3.93	2.71	4.00	3.35	3.49	4.14	2.89	4.12	2.78
MI	13.9	6.5	21.6	6.8	16.4	14.4	5.5	21.6	7.4	15.9

(c)

FIG. 11. Table depicting reconstructions, segmentations, and selected feature values for the (a) LAD1, (b) LAD2, and (c) LCX plaques (H66/G1) at phases $\bar{\phi}$ spanning two cardiac cycles. Values for 3D velocity VEL (mm/s), edge-based volume VOL-E (mm^3), mean intensity MEAN INT (HU), sphericity SPHER, average margin gradient MG, and motion index MI (mm/s) are given.

$\bar{\phi}$	0.30	0.50	0.70	0.89	1.09	1.29	1.49	1.68	1.88	2.08
Rec										
Seg										
VEL	36.9	8.4	82.3	15.5	74.0	48.7	1.2	77.2	25.2	44.0
VOL-E	107.6	79.7	104.0	85.2	125.2	114.4	58.5	165.0	84.8	141.1
SPHER	0.34	0.60	0.33	0.60	0.33	0.51	0.59	0.30	0.52	0.30
MEAN INT	124	143	118	141	109	106	183	96	123	111
MG	3.13	3.72	2.80	3.62	2.66	3.49	4.10	2.74	3.97	2.68
MI	45.7	21.3	70.9	22.3	53.9	47.4	18.1	71.1	24.4	52.2

(a)

$\bar{\phi}$	0.30	0.50	0.70	0.89	1.09	1.29	1.49	1.68	1.88	2.08
Rec										
Seg										
VEL	64.1	23.8	126.9	14.4	34.0	6.4	1.8	4.6	12.6	49.1
VOL-E	8.2	8.6	3.6	8.4	7.8	9.4	8.2	13.0	8.6	9.6
SPHER	0.41	0.46	0.00	0.38	0.24	0.36	0.42	0.21	0.47	0.30
MEAN INT	102	89	74	112	72	102	118	65	117	91
MG	3.42	2.92	2.57	3.48	3.33	2.69	3.54	3.91	3.23	3.16
MI	35.0	16.3	54.2	17.1	41.3	36.3	13.9	54.4	18.7	40.0

(b)

$\bar{\phi}$	0.30	0.50	0.70	0.89	1.09	1.29	1.49	1.68	1.88	2.08
Rec										
Seg										
VEL	13.1	8.7	119.7	22.5	109.2	56.7	20.9	29.5	2.5	17.4
VOL-E	53.9	46.9	61.8	70.8	54.3	76.3	40.9	117.3	43.0	10.4
SPHER	0.36	0.35	0.30	0.40	0.35	0.25	0.34	0.35	0.34	0.35
MEAN INT	101	116	88	88	91	76	120	79	127	159
MG	3.77	3.49	3.88	3.27	2.68	3.48	4.00	2.95	3.84	2.07
MI	42.8	19.8	66.7	18.0	47.8	44.5	16.8	66.8	20.0	46.2

(c)

FIG. 12. Table depicting reconstructions, segmentations, and selected feature values for the (a) RCA1, (b) RCA2, and (c) RCA3 plaques (H66/G1) at phases $\bar{\phi}$ spanning two cardiac cycles. Values for 3D velocity VEL (mm/s), edge-based volume VOL-E (mm^3), mean intensity MEAN INT (HU), sphericity SPHER, average margin gradient MG, and motion index MI (mm/s) are given.

III.C. Correlations of features to the plaque motion index

Figure 14 shows plots of two features (square root of 3D velocity and average margin gradient) versus the plaque motion index for the RCA1 plaque with the H66/G1 combination. These plots are shown to illustrate how these features varied with respect to the motion index. The motion index demonstrated a linear relationship with the 3D velocity square root and the average margin gradient. Respective Pearson's correlation coefficients were 0.888 and −0.790.

In Table IV, partial correlation coefficients between individual features and the plaque motion index for the six plaques are listed. Partial correlation coefficients using data from all six plaques are also included. Features with stronger correlations ($|r| \in [0.60, 1.00]$) for data encompassing all six plaques included 3D velocity, maximum intensity, and stan-

dard deviation of intensity. Mean intensity was a feature which demonstrated a stronger correlation with the motion index for each individual plaque. Other features, such as edge-based volume, threshold-based volume, sphericity, irregularity, average margin gradient, and variance of margin gradient had stronger correlations with motion index for some plaques but not others. Correlations for these features varied quite noticeably between different plaques. The minimum intensity feature exhibited a poor correlation with motion index. For the RCA1 and RCA2 plaques, the minimum intensity failed to show statistically significant correlations with the plaque motion index ($p > 0.05$ with respect to null hypotheses of zero correlations).

Partial correlation coefficients between features are listed in Table V. Of the 12 feature pairs with stronger correlations ($|r| \in [0.60, 1.00]$), ten of these involved intensity-based fea-
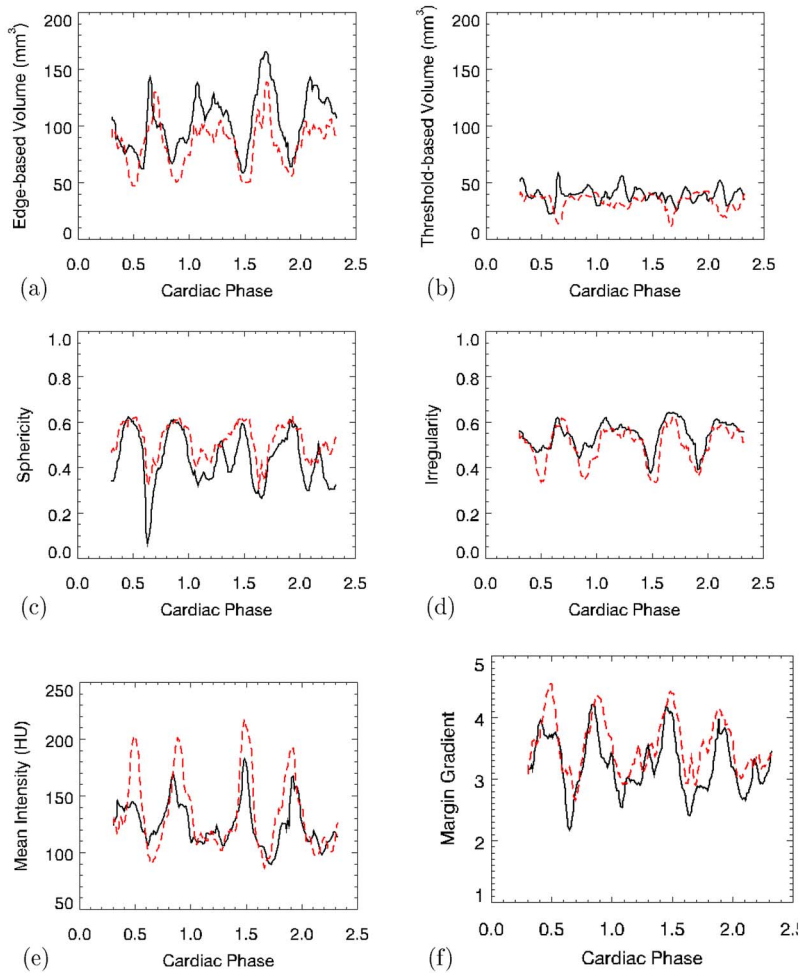
FIG. 13. Graphs showing relationships between phase-correlated features and cardiac phase for the RCA1 plaque (H66/G1). The phase-correlated features are (a) edge-based volume, (b) threshold-based volume, (c) sphericity, (d) irregularity, (e) mean intensity, and (f) average margin gradient. In each plot, the dark solid line represents features from single-sector gating, and the light dashed line represents features from two-sector gating. For comparison purposes, the actual volume of the plaque is 36.7 mm^3.

tures. Only the average margin gradient/variance of margin gradient and the edge-based volume/irregularity pairs did not include an intensity-based feature.

IV. DISCUSSION

In this study, methods for generating a comprehensive set of quantitative features that can be used to characterize motion artifacts affecting calcified plaques in noncontrast-enhanced cardiac CT scans have been discussed. These methods include the RP-ROI tracking algorithm for generating 4D sets of ROI images centered on calcified plaques as well as the segmentation and feature extraction techniques necessary for obtaining phase-correlated dynamic, morphological, and intensity-based features. As stated earlier, the methods introduced in this paper are being used for developing an automated scheme for evaluating calcified plaques in cardiac CT images with respect to motion artifacts.[22]

The RP-ROI algorithm introduced in this paper is important because it serves as a mechanism for obtaining the features that characterize calcified plaques in an automated manner directly from the projection data acquired during a cardiac CT scan. With respect to automation, the user only needs to specify the location of the plaque at an initial cardiac phase. The RP-ROI algorithm then automatically produces a series of small 4D ROI images centered on the plaque over multiple cardiac cycles. If this algorithm were not used, the user would need to specify the locations of plaques from images reconstructed at each cardiac phase of interest.

The algorithm's computational efficiency stems from its basic premise of using an edge-based segmentation method for dictating the location of the ROI image that is reconstructed at a subsequent cardiac phase. Since the approximate location of the plaque is known, smaller-sized ROIs whose lengths are on the order of a couple of centimeters can be reconstructed. As a result, more phase-correlated ROI images can be reconstructed in the same amount of time required to reconstruct a single image covering a much larger FOV. It is important to note that a similar method has been proposed in cardiac magnetic resonance imaging, in which image processing techniques are used to prospectively select locations of slices at which images are acquired during subsequent cardiac phases.[38,39]

However, the RP-ROI algorithm is susceptible to failure when tracking smaller plaques undergoing abrupt large-scale movements. For example, for the RCA3 plaque with the 80 bpm heart rate and three-sector gating combination, the segmentation algorithm was not capable of detecting the plaque over seven consecutive reconstructions. Fortunately, for this particular case, the algorithm was able to detect the

TABLE III. (a) Means and (b) standard deviations of features for individual calcified plaques. Feature identifiers are listed in Table II.

		VEL	ACC	VOL-E	VOL-T	SPHER	IRREG	MAX INT	MEAN INT	MIN INT	STD INT	MG	VMG
	LAD1	0.44	5.23	46.14	37.86	0.64	0.35	429.64	230.33	36.46	101.05	3.78	3.27
	LAD2	2.37	24.00	42.35	28.96	0.54	0.34	399.78	190.16	31.01	86.61	3.50	3.40
	LCX1	1.61	16.20	50.84	38.35	0.59	0.35	386.53	198.00	33.15	81.67	3.49	2.50
	RCA1	5.17	55.27	89.21	34.76	0.46	0.52	279.30	128.06	8.27	56.53	3.27	3.29
	RCA2	4.32	67.45	7.68	0.92	0.34	0.02	161.16	88.89	32.21	29.37	3.19	2.88
(a)	RCA3	4.90	72.46	56.26	11.08	0.33	0.45	236.07	98.43	7.78	48.67	3.30	3.86
		VEL	ACC	VOL-E	VOL-T	SPHER	IRREG	MAX INT	MEAN INT	MIN INT	STD INT	MG	VMG
	LAD1	0.28	3.76	3.45	1.51	0.01	0.02	13.40	13.79	9.33	4.68	0.13	0.49
	LAD2	1.60	18.38	9.76	3.09	0.07	0.06	42.47	29.27	13.22	14.82	0.36	0.81
	LCX1	0.98	11.20	13.16	6.35	0.04	0.07	41.61	29.59	17.42	13.35	0.50	0.74
	RCA1	3.66	45.64	23.20	10.26	0.13	0.07	71.28	27.51	16.37	19.23	0.48	1.53
	RCA2	4.08	54.53	2.29	0.99	0.12	0.12	46.36	16.13	9.48	10.94	0.36	1.22
(b)	RAC3	4.81	68.45	21.85	5.43	0.08	0.13	64.17	26.14	28.88	17.80	0.57	2.09

plaque on the eighth reconstruction. However, more intelligent methods involving adaptive modifications of the segmentation parameters may be needed to increase the robustness of the RP-ROI algorithm.

The RP-ROI algorithm requires the presence of a continuous phase-correlated projection dataset from which images can be reconstructed in a retrospective fashion. However, images obtained for CAC scoring applications are most often obtained in a prospective fashion, in which images can be reconstructed only during a small portion of the cardiac cycle due to the small time window spanned by the projection dataset. Although the RP-ROI algorithm, as discussed in this paper, cannot be used for these datasets, the RP-ROI algorithm potentially can be applied to datasets which allow for retrospective reconstruction including those acquired through low-dose methods.[40,41]

In terms of future work, the RP-ROI algorithm could be applied toward cases of multiple calcified plaques located along a short segment of the coronary artery. These cases are commonly found in patients with more severe coronary artery disease. Applying the RP-ROI algorithm to these cases would be more challenging, as multiple seed points within a small region would be needed. The RP-ROI algorithm could also play a valuable role in applications involving contrast-enhanced CTA, in which specific coronary landmarks at mul-

tiple phases throughout the cardiac cycle may be reconstructed with minimal user interaction. However, segmenting and registering coronary landmarks at multiple phases in the presence of motion artifacts would be a much more difficult task. In addition, the algorithm would need to handle cardiac scans incorporating ECG-dose modulation, in which the tube current is decreased during phases of higher cardiac motion.[42]

With respect to the features, previous studies have used individual features, such as plaque contrast[16] and velocity,[17] for characterizing the motion artifacts affecting coronary structures. However, this paper evaluates a more comprehensive set of features (Table II) that can be used to characterize motion artifacts. In particular, properties of the plaque such as its kinetics, volume, shape, margin sharpness, and intensity, can be described by the two dynamic, six morphological, and four intensity-based features discussed in this paper.

In terms of values for individual features, edge-based volumes were always greater than threshold-based volumes (see Table III and Figs. 13(a) and 13(b)) for the following reasons. First, edge-based segmentation results often included pixels whose intensities were lower than the 130 HU used for obtaining the threshold-based segmentations. Second, as

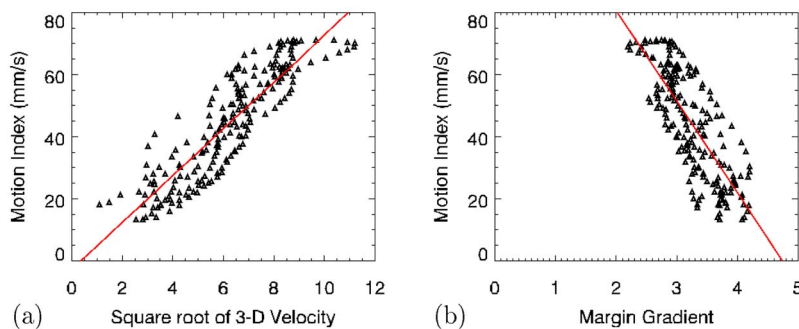(a)   Square root of 3-D Velocity

(b)   Margin Gradient

FIG. 14. Graphs showing the relationships between selected features and the plaque motion index for the RCA1 plaque (H66/G1). In (a), the square root of 3D velocity (VEL) is plotted against motion index. In (b), average margin gradient (MG) is plotted against motion index. Linear regression lines are included in both plots. Corresponding Pearson's correlation coefficients are 0.888 and −0.790, respectively.

TABLE IV. Correlations between features and the plaque motion index. Partial correlation coefficients, which were adjusted for heart rate, number of gated sectors, and mean feature values, are reported for individual plaques and across all six plaques (ALL). Features with stronger correlations ($|r| \in [0.600, 1.000]$) are in bold. Correlations with single asterisks (*) correspond to p-values $p \in [0.001, 0.050]$. Correlations with double asterisks (**) correspond to $p > 0.050$. P-values are defined with respect to null hypotheses of zero correlations. Feature identifiers are listed in Table II.

	VEL	ACC	VOL-E	VOL-T	SPHER	IRREG	MAX INT	MEAN INT	MIN INT	STD INT	MG	VMG
LAD1	**0.788**	0.227	**0.656**	0.320	0.286	0.402	0.063	**−0.764**	−0.365	−0.459	−0.569	0.479
LAD2	**0.819**	0.121	**0.773**	0.526	**−0.822**	**0.814**	**−0.692**	**−0.885**	−0.412	**−0.831**	**−0.832**	−0.153
LCX1	**0.864**	0.100	**0.802**	0.578	−0.496	**0.816**	**−0.747**	**−0.862**	−0.523	**−0.761**	**−0.838**	−0.131
RCA1	**0.836**	0.201	0.505	−0.530	**−0.746**	**0.651**	**−0.766**	**−0.722**	0.033**	**−0.784**	**−0.716**	**−0.607**
RCA2	0.521	0.374	−0.200	**−0.643**	−0.332	−0.258	−0.588	**−0.604**	−0.033**	**−0.620**	−0.055*	−0.097
RCA3	**0.691**	0.461	0.369	**−0.753**	−0.126	0.208	**−0.737**	**−0.609**	−0.125	**−0.703**	−0.447	−0.504
ALL	**0.664**	0.322	0.408	−0.334	−0.490	0.219	**−0.680**	−0.566	−0.090	**−0.677**	−0.471	−0.410

discussed in Sec. II B 2, all pixel values included in the threshold-based segmentation result were also included in the edge-based segmentation results.

For small plaques such as the RCA2 plaque, sphericity and irregularity features sometimes fell outside of the range of acceptable values. For example, as seen in Fig. 12(b), the RCA2 plaque at a phase $\phi = 0.70$ had a sphericity of 0.00. In this particular case, the plaque consisted of two major fragments, and the center of mass for this plaque fell directly between these two fragments. Since the volume of this plaque was extremely small, the sphere of effective diameter d_{eff} used to calculate sphericity failed to cover any voxels corresponding to these two fragments. In Table III(a), the extremely low mean irregularity of 0.02 for the RCA2 plaque as well as its standard deviation of 0.12 highlights the fact that irregularity values for the RCA2 plaque at many cardiac phases were negative. The RCA2 plaque was very thin, and its width often spanned only a single voxel. As a result, the surface area was abnormally low and resulted in a negative irregularity value. Negative irregularity values were also obtained during phases at which small plaques exhibited a high sphericity. Alternative methods for calculating sphericity and irregularity based on numbers of exposed edges

instead of numbers of voxels may prevent the acquisition of negative irregularity values for small plaques.

In this study, partial correlation coefficients adjusted for heart rate, numbers of gated sectors, and mean feature values of the six plaques were used to evaluate the strengths of associations between individual features and the plaque motion index. As shown in Table IV, the partial correlation coefficients for a given feature and the motion index varied rather substantially between different plaques. For the RCA2 plaque, for example, edge-based volume and irregularity features exhibited negative correlations with plaque motion, whereas for the other five plaques these two features demonstrated positive correlations. In terms of the partial correlation coefficients using data from all six plaques, the 3D velocity, maximum intensity, and standard deviation of intensity exhibited stronger correlations ($|r| \in [0.60, 1.00]$) with the plaque motion index, whereas the minimum intensity correlation demonstrated the weakest correlation. In terms of correlations between different features (Table V), many of the stronger feature-to-feature correlations ($|r| \in [0.60, 1.00]$) involved intensity-based features (maximum intensity, mean intensity, and standard deviation of intensity)

TABLE V. Correlations between individual features. Partial correlation coefficients, which were adjusted for heart rate, number of gated sectors, and mean feature values, are reported using data from all six plaques. Features with stronger correlations ($|r| \in [0.600, 1.000]$) are in bold. Correlations with single asterisks (*) correspond to p-values $p \in [0.001, 0.050]$. Correlations with double asterisks (**) correspond to $p > 0.050$. P-values are defined with respect to null hypotheses of zero correlations. Feature identifiers are listed in Table II.

	VEL	ACC	VOL-E	VOL-T	SPHER	IRREG	MAX INT	MEAN INT	MIN INT	STD INT	MG	VMG
VEL												
ACC	0.217											
VOL-E	0.360	−0.136										
VOL-T	−0.254	−0.144	0.144									
SPHER	−0.472	0.024*	−0.393	0.133								
IRREG	0.177	−0.044	**0.682**	0.055	−0.292							
MAX INT	**−0.631**	−0.053	−0.500	0.275	0.520	−0.258						
MEAN INT	−0.585	−0.002**	**−0.655**	0.136	0.546	−0.540	**0.733**					
MIN INT	−0.135	0.038	−0.429	−0.020*	0.157	−0.504	0.166	0.522				
STD INT	**−0.640**	−0.028	−0.513	0.168	0.527	−0.261	**0.929**	**0.744**	0.046			
MG	−0.517	0.013**	−0.362	−0.020*	0.378	−0.103	**0.690**	0.553	−0.095	**0.801**		
VMG	−0.389	0.008**	−0.187	0.230	0.178	0.067	**0.692**	0.222	−0.205	**0.686**	**0.666**	

being correlated with each other as well as with other features including 3D velocity, edge-based volume, average margin gradient, and variance of margin gradient. Only two feature pairs (edge-based volume/irregularity and average margin gradient/variance of margin gradient) had stronger correlations that did not include intensity-based features.

Although the feature-motion index correlations and feature-feature correlations discussed in this paper provide useful information regarding how strongly these indices were associated with one another, these coefficients were based on six simulated calcified plaques. Our future work includes applying the methodologies presented in this paper to calcified plaques from clinical datasets. In particular, methods for characterizing calcified plaques from both prospective and retrospective scans will be examined.

ACKNOWLEDGMENTS

[a] Electronic mail: mtking@uchicago.edu

[1] T. Fuchs, M. Kachelriess, and W. A. Kalender, "Technical advances in multi-slice spiral CT," Eur. J. Radiol. **36**, 69–73 (2000).

[2] M. Kachelriess, S. Ulzheimer, and W. A. Kalender, "ECG-correlated image reconstruction from subsecond multi-slice spiral CT scans of the heart," Med. Phys. **27**, 1881–1902 (2000).

[3] M. Kachelriess, S. Ulzheimer, and W. A. Kalender, "ECG-correlated imaging of the heart with subsecond multislice spiral CT," IEEE Trans. Med. Imaging **19**, 888–901 (2000).

[4] T. Flohr and B. Ohnesorge, "Heart rate adaptive optimization of spatial and temporal resolution for electrocardiogram-gated multislice spiral CT of the heart," J. Comput. Assist. Tomogr. **25**, 907–923 (2001).

[5] T. G. Flohr, U. J. Schoepf, A. Kuettner, S. Halliburton, H. Bruder, C. Suess, B. Schmidt, L. Hofmann, E. K. Yucel, S. Schaller, and B. Ohnesorge, "Advances in cardiac imaging with 16-section CT systems," Acad. Radiol. **10**, 386–401 (2003).

[6] J. Horiguchi, T. Nakanishi, A. Tamura, and K. Ito, "Coronary artery calcium scoring using multicardiac computed tomography," J. Comput. Assist. Tomogr. **26**, 880–885 (2002).

[7] P. Schoenhagen, S. S. Halliburton, A. E. Stillman, S. A. Kuzmiak, S. E. Nissen, E. M. Tuzcu, and R. D. White, "Noninvasive imaging of coronary arteries: Current and future role of multi-detector row CT," Radiology **232**, 7–17 (2004).

[8] C. H. McCollough, M. R. Bruesewitz, T. R. Daly, and F. E. Zink, "Motion artifacts in subsecond conventional CT and electron-beam CT: Pictorial demonstration of temporal resolution," Radiographics **20**, 1675–1681 (2000).

[9] S. Mao, M. Budoff, H. Bakhsheshi, and S. Liu, "Improved reproducibility of coronary artery calcium scoring by electron beam tomography with a new electrocardiographic trigger method," Invest. Radiol. **36**, 363–367 (2001).

[10] R. Detrano, M. Anderson, J. Nelson, N. Wong, J. Carr, M. McNitt-Gray, and D. Bild, "Coronary calcium measurements: Effect of CT scanner type and calcium measure on rescan reproducibility-MESA study," Radiology **236**, 477–484 (2005).

[11] J. Horiguchi, H. Fukuda, H. Yamamoto, N. Hirai, F. Alam, H. Kakizawa, M. Hieda, T. Tachikake, K. Marukawa, and K. Ito, "The impact of motion artifacts on the reproducibility of repeated coronary artery calcium measurements," Eur. Radiol. **17**, 81–86 (2007).

[12] K. Nieman, M. Oudkerk, B. Rensing, P. van Ooijen, A. Munne, R. van Geuns, and P. de Feyter, "Coronary angiography with multi-slice computed tomography," Lancet **357**, 599–603 (2001).

[13] D. Ropers, U. Baum, K. Pohle, K. Anders, S. Ulzheimer, B. Ohnesorge, C. Schlundt, W. Bautz, W. Daniel, and S. Achenbach, "Detection of coronary artery stenoses with thin-slice multi-detector row spiral computed tomography and multiplanar reconstruction," Circulation **107**, 664–666 (2003).

[14] G. L. Raff, M. J. Gallagher, W. W. O'Neill, and J. A. Goldstein, "Diagnostic accuracy of noninvasive coronary angiography using 64-slice spiral computed tomography," J. Am. Coll. Cardiol. **46**, 552–557 (2005).

[15] A. W. Leber, A. Knez, F. von Ziegler, A. Becker, K. Nikolaou, S. Paul, B. Wintersperger, M. Reiser, C. R. Becker, G. Steinbeck, and P. Boekstegers, "Quantification of obstructive and nonobstructive coronary lesions by 64-slice computed tomography: A comparative study with quantitative coronary angiography and intravascular ultrasound," J. Am. Coll. Cardiol. **46**, 147–154 (2005).

[16] W. P. Segars, K. Taguchi, G. S. K. Fung, E. K. Fishman, and B. M. W. Tsui, "Effect of heart rate on CT angiography using the enhanced cardiac model of the 4D NCAT," Proc. SPIE **6142**, 18 (2006).

[17] M. Vembar, M. Garcia, D. Heuscher, R. Haberl, D. Matthews, G. Bohme, and N. Greenberg, "A dynamic approach to identifying desired physiological phases for cardiac imaging using multislice spiral CT," Med. Phys. **30**, 1683–1693 (2003).

[18] M. King, M. Giger, and X. Pan, "Investigation of calcified coronary plaque tracking in cardiac CT," In *Conf. Rec. 2006 IEEE Nuclear Science Symp. Medical Imaging Conference*, San Diego (2006).

[19] K. G. Gilhuijs, M. L. Giger, and U. Bick, "Automated analysis of breast lesions in three dimensions using dynamic magnetic-resonance imaging," Med. Phys. **25**, 1647–1654 (1998).

[20] Z. Huo, M. L. Giger, C. J. Vyborny, D. E. Wolverton, R. A. Schmidt, and K. Doi, "Automated computerized classification of malignant and benign mass lesions on digitized mammograms," Acad. Radiol. **5**, 155–168 (1998).

[21] W. Chen, M. L. Giger, L. Lan, and U. Bick, "Computerized interpretation of breast MRI: Investigation of enhancement-variant dynamics," Med. Phys. **31**, 1076–1082 (2004).

[22] M. King, M. Giger, K. Suzuki, D. Bardo, B. Greenberg, L. Lan, and X. Pan, "Computerized assessment of motion-contaminated calcified plaques in cardiac multidetector CT," Med. Phys. **34**, 4876–4889 (2007).

[23] W. P. Segars, D. S. Lalush, and B. M. W. Tsui, "A realistic spline-based dynamic heart phantom," IEEE Trans. Nucl. Sci. **46**, 503–506 (1999).

[24] W. P. Segars, Ph.D. thesis, The University of North Carolina, 2001.

[25] J. M. Garrity, W. P. Segars, S. B. Knisley, and B. M. W. Tsui, "Development of a dynamic model for the lung lobes and airway tree in the NCAT phantom," IEEE Trans. Nucl. Sci. **50**, 378–383 (2003).

[26] M. Grass, T. Köhler, and R. Proksa, "Angular weighted hybrid cone-beam CT reconstruction for circular trajectories," Phys. Med. Biol. **46**, 1595–1610 (2001).

[27] P. J. LaRiviere, "Penalized-likelihood sinogram smoothing for low-dose CT," Med. Phys. **32**, 1676–1683 (2005).

[28] F. Noo, M. Defrise, R. Clackdoyle, and H. Kudo, "Image reconstruction from fan-beam projections on less than a short scan," Phys. Med. Biol. **47**, 2525–2546 (2002).

[29] X. Pan, D. Xia, Y. Zou, and L. Yu, "A unified analysis of FBP-based algorithms in circular cone- and fan-beam scans," Phys. Med. Biol. **49**, 4349–4369 (2004).

[30] L. A. Feldkamp, L. C. Davis, and J. W. Kress, "Practical cone-beam algorithm," J. Opt. Soc. Am. A **1**, 612–619 (1984).

[31] G. Wang, T.-H. Lin, P. Cheng, and D. M. Shinozaki, "A general cone-beam reconstruction algorithm," IEEE Trans. Med. Imaging **12**, 486–496 (1993).

[32] K. Taguchi, B. S. Chiang, and I. A. Hein, "Direct cone-beam cardiac reconstruction algorithm with cardiac banding artifact correction," Med. Phys. **33**, 521–539 (2006).

[33] M. Sonka, V. Hlavac, and R. Boyle, *Image Processing, Analysis, and Machine Vision* (Brooks Cole, Pacific Grove, CA, 1999).

[34] W. K. Pratt, *Digital Image Processing*, 3rd ed. (Wiley, New York, 2001).

[35] T. Q. Callister, B. Cooil, S. Raya, N. J. Lippolis, D. J. Russo, and P. Raggi, "Coronary artery disease: Improved reproducibility of calcium

scoring with an electron-beam CT volumetric method," Radiology **208**, 807–814 (1998).

[36] D. J. Cowden, "The multiple-partial correlation coefficient," J. Am. Stat. Assoc. **47**, 442–456 (1952).

[37] J. Cohen, P. Cohen, S. G. West, and L. S. Aiken, *Applied Multiple Regression/Correlation Analysis for the Behavioral Sciences*, 3rd ed. (Lawrence Erlbaum, Mahwah, NJ, 2003).

[38] T. K. Foo, V. B. Ho, and M. N. Hood, "Vessel tracking: Prospective adjustment of section-selective MR angiographic locations for improved coronary artery visualization over the cardiac cycle," Radiology **214**, 283–289 (2000).

[39] M. Saranathan, V. B. Ho, M. N. Hood, T. K. Foo, and C. J. Hardy, "Adaptive vessel tracking: Automated computation of vessel trajectories for improved efficiency in 2D coronary MR angiography," J. Magn. Re-son Imaging **14**, 368–373 (2001).

[40] B. Ohnesorge, T. Flohr, R. Fischbach, A. F. Kopp, A. Knez, S. Schroeder, U. J. Schoepf, A. Crispin, E. Klotz, M. F. Reiser, and C. R. Becker, "Reproducibility of coronary calcium quantification in repeat examinations with restrospectively ECG-gated multisection spiral CT," Eur. Radiol. **12**, 1532–1540 (2002).

[41] J. Horiguchi, H. Yamamoto, N. Hirai, Y. Akiyama, C. Fujioka, K. Marukawa, H. Fukuda, and K. Ito, "Variability of repeated coronary artery calcium measurements on low-dose ECG-gated 16-MDCT," AJR, Am. J. Roentgenol. **187**, W1–W6 (2006).

[42] T. F. Jakobs, C. R. Becker, B. Ohnesorge, T. Flohr, C. Suess, U. J. Schoepf, and M. F. Reiser, "Multislice helical CT of the heart with retro-spective ECG gating: Reduction of radiation exposure by ECG-controlled tube current modulation," Eur. Radiol. **12**, 1081–1086 (2002).